Volume 12
Number 48
28 December 2024
Pages 12403–12686

Journal of
Materials Chemistry B

Materials for biology and medicine

rsc.li/materials-b

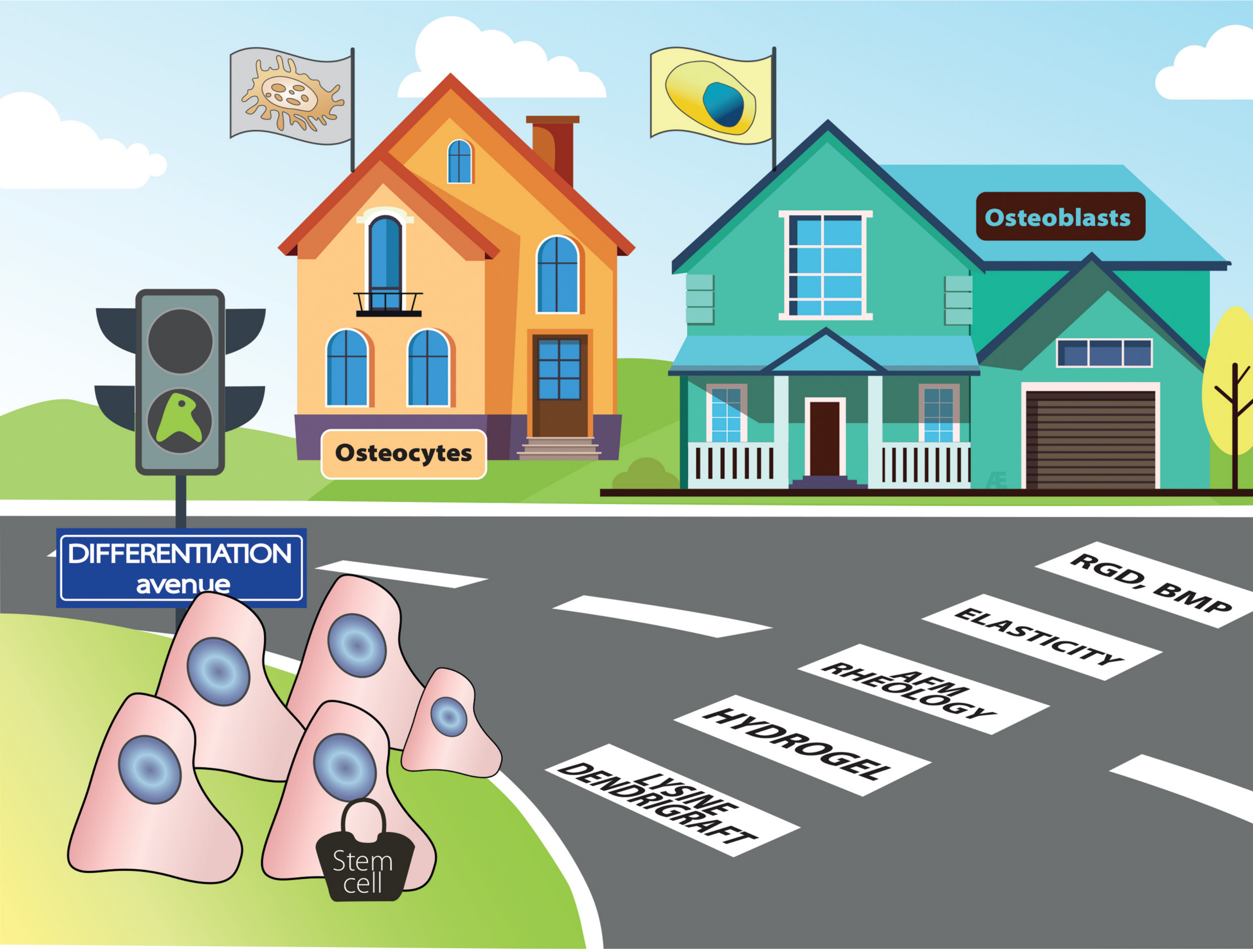

ISSN 2050-750X

ROYAL SOCIETY
OF **CHEMISTRY**

PAPER

Marie-Christine Durrieu *et al.*

Bioactive hydrogels based on lysine dendrigrafts as crosslinkers: tailoring elastic properties to influence hMSC osteogenic differentiation

Journal of
Materials Chemistry B

PAPER

View Article Online
View Journal | View Issue

Cite this: *J. Mater. Chem. B*, 2024, **12**, 12508

Bioactive hydrogels based on lysine dendrigrafts as crosslinkers: tailoring elastic properties to influence hMSC osteogenic differentiation†

Michele Valeo,[a] Sébastien Marie,[b] Murielle Rémy,[a] Tiphaine Menguy,[b] Cédric Le Coz,[c] Michael Molinari,[a] Cécile Feuillie,[a] Fabien Granier[b] and Marie-Christine Durrieu *[a]

Received 19th July 2024,
Accepted 17th October 2024

DOI: 10.1039/d4tb01578a

rsc.li/materials-b

Dendrigrafts are multivalent macromolecules with less ordered topology and higher branching than dendrimers. Exhibiting a high density of terminal amines, poly-L-lysine dendrigrafts of the fifth generation (DGL G5) allow hydrogel formation with tailorable crosslinking density and surface modification. This work presents DGL G5 as multifunctional crosslinkers in biomimetic PEG hydrogels to favour the osteogenic differentiation of human mesenchymal stem cells (hMSCs). DGL G5 reaction with dicarboxylic-acid PEG chains yielded amide networks of variable stiffness, measured at the macro and surface nanoscale. Oscillatory rheometry and compression afforded consistent values of Young's modulus, increasing from 8 to more than 30 kPa and correlating with DGL G5 concentration. At the surface level, AFM measurements showed the same tendency but higher E values, from approximately 15 to more than 100 kPa, respectively. To promote cell adhesion and differentiation, the hydrogels were functionalised with a GRGDSPC peptide and a biomimetic of the bone morphogenetic protein 2 (BMP-2), ensuring the same grafting concentrations (between 2.15 ± 0.54 and 2.28 ± 0.23 pmols mm^{-2}) but different hydrogel stiffness. 6 h after seeding on functionalised hydrogels in serum-less media, hMSC showed nascent adhesions on the stiffer gels and greater spreading than on glass controls with serum. After two weeks in osteogenic media, hMSC seeded on the stiffer gels showed greater spreading, more polygonal morphologies and increased levels of osteopontin, an osteoblast marker, compared to controls, which peaked on 22 kPa-gels. Together, these results demonstrate that DGL G5-PEG hydrogel bioactivity can influence the adhesion, spreading and early commitment of hMSCs.

Introduction

The extracellular matrix (ECM) is an essential component of the cell microenvironment, presenting elaborated compositions and highly tissue-specific properties.[1] Cells attach to the matrix *via* adhesion receptors, like integrins, arranged in membrane complexes linked to the actomyosin architecture of the cytoskeleton.[2,3] These focal adhesions control cytosolic tension and act as mechanosensors that propagate forces to and from the matrix, enabling cells to sense the mechanical or topographical features of the local microenvironment.[2] Cellular mechanosensing of the environment properties emerged as one of the main regulators of cell behaviour, modulating – among others – cell adhesion and spreading,[4] migration[5] and differentiation towards specific lineages.[6] Notably, matrix stiffness was shown to play a central role in controlling the differentiation fate[7] of adult stem cells like mesenchymal stem cells (hMSCs).[8,9] hMSCs are bone marrow-derived, multipotent cells capable of differentiating along multiple mesenchymal lineages,[10] including cartilage, bone, and fat cells, that have been extensively investigated to decipher the role of mechanotransduction in bone cell differentiation and development.[11] Recent studies have shown that substrate stiffness induces hMSC osteogenic differentiation by reinforcing focal adhesions and increasing cytosolic tension, which ultimately regulate the mechanosensitive translocation of osteogenic transcription factors into the cell nucleus.[3] On 2D[12,13] and 3D matrices,[14,15] the stiffness required for hMSC differentiation to cells of the bone lineage is reported, in the literature, in a range from 20 kPa to at least 115 kPa in Young's modulus (E),[12,14,16,17] sometimes with contradictory results due to the use of different

---

[a] *Université de Bordeaux, CNRS, Bordeaux INP, CBMN, UMR 5248, F-33600 Pessac, France. E-mail: marie-christine.durrieu@inserm.fr*
[b] *FGHI, Montarnaud, France*
[c] *Université de Bordeaux, CNRS, Bordeaux INP, LCPO, ENSMAC, F-33600 Pessac, France*

† Electronic supplementary information (ESI) available. See DOI: **https://doi.org/10.1039/d4tb01578a**

techniques for the mechanical characterisation.[12,18,19] Nevertheless, with rising demand for bone grafts, the limited implantability and regenerative capacity of skeletal tissues, and the shortcomings of autologous grafting,[20] biomaterial engineering for bone tissue regeneration is currently at the centre of intensive research. For this purpose, developing engineered matrices with controllable mechanical and biochemical properties can provide valuable insights into the fundamental functioning of mechanotransduction processes involved, for example, in bone cell differentiation. Hydrogels, consisting of crosslinked polymer networks swollen in water, are ECM-mimicking biomaterials extensively used to characterise hMSC differentiation in response to specific material clues.[21,22] The covalent functionalisation of synthetic hydrogels allows the controlled tethering of biochemical clues, mimicking the presentation of matrix-bound ligands to promote cell adhesion, proliferation or differentiation.[13,23,24] Among biomolecules used to control cell differentiation, the bone morphogenetic protein 2 (BMP-2) is a growth factor widely used in bone tissue engineering for its osteogenic activity.[25] Binding to cell surface receptors, the BMPR-I and II, the BMP-2 and the biomimetic peptides derived from its knuckle-epitope[26,27] can induce hMSC osteogenic differentiation and matrix deposition *in vitro*[25,28] and ectopic bone formation and calcification *in vivo*,[26,29] provided in the soluble[30] or immobilised form.[14,31,32] BMP-2 tethering reduces the amount of protein required and the side effects associated with its diffusion *in vivo*,[29] allowing the precise control of its spatial distribution. Moreover, surface-bound BMP-2 enhances stiffness-mediated focal adhesion formation[25,30,33] by interacting with fibronectin-binding integrin subtypes, which – in turn – modulate BMP-2-initiated signalling in a synergistic crosstalk.[31,34,35] As of now, most methods to fabricate stiff PEG hydrogels[22,36,37] rely on acrylate-based photo-polymerization, which allows rapid crosslinking, confined network formation and broad-range adaptability of hydrogel stiffness (1–1000 kPa). However, photochemical reactions are limited by UV light penetration depth, the use of radical initiators and the formation of more network defects.[22,38] Alternatively, having high surface densities of functional end-groups, dendritic polymers can be used as multifunctional crosslinkers allowing control over the hydrogel's mechanical properties and surface functionalisation.[39,40] Dendrimers are highly branched macromolecules synthesised in generations (G) by the iterative addition of branched layers around a core unit.[41] As the number of branching units and functional groups increases at each generation, dendrimers have controllable size, polymerisation degree, end-group functionality, and surface charge. Amine-terminated dendrimers, like poly(amidoamine) (PAMAM), can be modified with various end-group functionalisation strategies to decrease the cytotoxic effects of high surface charge,[42,43] allowing their use in biological applications.[44–46] Poly-L-lysine dendrigrafts (DGLs) are a less explored class of aminated hyper-branched polymers exhibiting more disordered topology than dendrimers but also higher branching and functional end-group density.[47,48] DGLs, obtained by ring-opening polymerisation (ROP) of L-lysine-*N*-carboxyanhydrides (L-Lys-(NCA)) in four generations (G2-G5, the first generation G1 being the core and linear oligo-L-lysine), are highly water soluble, biodegradable and non-immunogenic.[49] Lysine dendrigrafts of the fifth generation (DGL G5) contain approximately 1000 lysines, exhibiting either free α-NH_2 groups (30%) or free ε-NH_2 (70%), partially hindered by steric crowding.[50,51] Having the possibility to form multiple bonds, DGL G5 are potentially useful hydrogel crosslinkers but have never been used for this application thus far.[52–54] Therefore, this study describes for the first time the use of DGL G5 dendrigrafts in PEG hydrogels with tunable stiffness, characterised by multiple techniques at the macro- and surface nanoscale. The hydrogels were functionalised for cell experiments with a combination of RGD-containing and BMP-2 biomimetic peptides, grafted using a maleimide-PEG-NHS spacer. After assessing the potential release of free DGL G5 from the crosslinked hydrogels with an *in vitro* assay, we evaluated hMSC adhesion to the functionalised DGL G5-PEG hydrogels after 6 h and the progress of osteogenic commitment by measuring hMSC morphology and osteopontin (OPN) expression after two weeks in osteogenic medium.[55]

Materials and methods

Materials

All reagents, if not specified elsewhere, were purchased from Sigma-Aldrich (USA), including α,ω-bis{2-[(3-carboxy-1-oxopropyl)-amino]ethyl}polyethylene glycol (Mr 2000, henceforth dicarboxylic acid-PEG) and MAL-dPEG®$_{24}$-NHS ester (Mal-PEG-NHS spacer). *N*-(3-Dimethylaminopropyl)-*N*′-ethylcarbodiimide hydrochloride (EDC) was obtained from ThermoFisher (USA). DGL G5 were obtained from Colcom (France). The RGD-containing peptide (GRGDSPC), *per se* or fluorescently labelled (GRGDSPC-TAMRA), was synthesised by GeneCust (France). The BMP-2 biomimetic peptide (BMP-2-bp) KRKIPKASSVPTELSAISMLYLC, containing a modified sequence of residues 73-92 of the BMP-2 knuckle epitope (KRKIPKASSVPTELSAISMLYLC), was synthesised as such or TAMRA-conjugated (henceforth BMP-2 bp or BMP-2-TAMRA bp, respectively) by GeneCust (France). Bone marrow-derived hMSCs and hMSC growth medium were obtained from Promocell (Germany). OsteoLife osteogenic differentiation medium without phenol red (to avoid interference during fluorescence immunostaining) was purchased from Lifeline Cell Tech. (USA). For immunostaining: the primary antibody anti-vinculin (V3191, mouse mAb) was obtained from Sigma-Aldrich (USA). The primary antibody anti-osteopontin (anti-OPN, AKm2A1, mouse mAb) was obtained from Santa Cruz Biotech. (USA). Alexa Fluor™ 488 Phalloidin (A12379) and the secondary antibodies Alexa Fluor™ 647 goat anti-mouse (IgG H + L, A21235) and 568 rabbit anti-mouse (A11061) were bought from Invitrogen (USA). DAPI (62248, 1 mg mM^{-1} solution), DMEM without Red Phenol, PBS, trypsin/EDTA, penicillin/streptomycin antibiotic solution, fetal bovine serum (FBS) and 16% paraformaldehyde (PFA) were obtained from Thermo Fisher (USA).

Methods

Synthesis of DGL G5-PEG hydrogels

DGL G5-PEG hydrogels were synthesised by forming amide bonds between dicarboxylic acid–PEG chains and amine-terminated DGL G5. Stock solutions were prepared separately by dissolving dicarboxylic acid–PEG in PBS at 400 mg mL^{-1} and DGL G5 in water at 275 mg mL^{-1}. The final concentration of dicarboxylic acid–PEG in the hydrogel mixture was fixed at 50 mM (100 mg mL^{-1}) or 65 mM (130 mg mL^{-1}). Then, the concentration of DGL G5 was varied to adjust the stoichiometry of the crosslinking reaction (the NH_2/COOH molar ratio, varied from 3 to 6). Before adding EDC solubilized in water (3-fold molar excess) to activate the carboxylic groups and trigger hydrogel formation, the pH was adjusted to 5 (using HCl or NaOH solutions). The liquid hydrogel mixture was vortexed and cast into Silicone Isolators™ (Grace Bio-Labs, USA) placed on a glass slide, yielding flat, 1 mm-thick hydrogel discs. The as-prepared hydrogels were rinsed with 70% v/v aqueous ethanol overnight and stored in sterile-filtered PBS at 4 °C until further use. Each DGL–PEG hydrogel formulation was denoted by the PEG concentration (50 or 65 mM) and the NH_2/COOH ratio (3–6). Four conditions were selected for the present study, named 65 mM-3, 50 mM-5, 65 mM-4 and 65 mM-5 (see Table S1, ESI† for all the formulations obtained).

Structural characterisation by ATR-FT IR spectroscopy

Fourier transform infrared absorption spectra were recorded in attenuated total reflectance (ATR) mode with a Nicholet iS50 – FTIR instrument, in the 4000–900 cm^{-1} region, averaging 100 scans with a 4 cm^{-1} resolution. The measurements were conducted at room temperature, using a Germanium crystal at 0° polarisation angle. After polymerisation, hydrogels were immersed in 0.1 M aqueous HCl to remove TFA salts and freeze-dried for three days. Spectra are reported (after manual baseline subtraction) in the 2300–1000 cm^{-1} range.

Equilibrium swelling experiments

After crosslinking (t_1), DGL G5-PEG gels were swollen in PBS at room temperature and weighed multiple times until a steady weight was reached (W_E). Then, swollen gels were lyophilised to measure the dry polymer weight (W_0). The swelling ratio at the timepoint t (Q_t), expressing the grams of PBS absorbed by each gram of dry polymer, was calculated according to the following equation:

$$Q_t = \frac{(W_t - W_0)}{W_0} \tag{1}$$

were W_t is the weight of the swollen gel at the time point t. The swelling ratio at equilibrium (Q_E), calculated using W_E, was measured for at least three separate samples per condition.

Shear oscillatory rheometry

Hydrogels were polymerised between the plates of an Anton Parr MCR301 rheometer with CP25/2 geometries for rheometry measurements before swelling. After a strain sweep to identify the linear viscoelastic region, storage (G') and loss (G'') moduli were recorded at room temperature, at 1% shear strain and 1 Hz oscillation frequency to follow the crosslinking time. When steady G' values were reached, frequency sweeps were collected between 0.1 and 10 Hz (consistent G' values indicated no plastic deformation occurred). For the analysis after swelling, pre-swollen gels were trimmed with a hollow puncher to fit in an 8 mm, Peltier cross-hatched plate-plate geometry of an HR10 hybrid rheometer (TA Instruments Inc.), applying a 0.2 N axial force to hold the hydrogels in place and avoid slipping during the analysis. Frequency sweeps were collected between 0.01 and 15 Hz (corresponding to 0.1 and 100 rad s^{-1}, respectively) at 2% shear oscillatory strain. Before and after swelling, each measurement was done in triplicate on independently prepared samples. For testing the validity of Young's modulus (E) theoretical calculations based on rheometrical data for DGL G5-PEG hydrogels, the complex modulus (G^*) was approximated to the value of G' (considering that G'' is negligible) and the following equation was used:

$$E = 2G'(1 + \nu) \tag{2}$$

where ν is the Poisson ratio of the material (the ratio of longitudinal to axial deformation), usually taken as 0.5 for covalent hydrogels.

Compression tests

An HR10 hybrid rheometer (TA Instruments Inc.) was used for compression tests. Pre-swollen gels were cut with a puncher before loading and analysed in an 8 mm, Peltier cross-hatched plate-plate geometry. The gels were deformed at a 1 mm per minute compression rate. Young's modulus (E) was calculated by fitting the stress–strain curves in its linear part (7% max deformation), analysing three independent samples per condition.

Atomic force microscopy (AFM)

Apparent Young's modulus (E) was measured on a Bioscope Resolve™ (Bruker, USA) atomic force microscope using force spectroscopy measurements. Considering that our samples are 1–2 mm thick, to avoid any ambiguity between the rheology and AFM measurements we refer to the apparent Young's modulus measured in AFM (over a few hundreds of nm) as the ''surface'' Young's modulus. PBS-swollen hydrogels were fixed to plastic Petri dishes using 1% aqueous agarose. Two probe geometries were used for force spectroscopy of unfunctionalised hydrogels. A sharp pyramidal tip allowed the probing of the sample's local mechanical properties, and a spherical silica bead, which deforms a larger part of the sample. The cantilever spring constant was calibrated with the thermal noise method and optical sensitivity was calibrated using a glass slide. The spherical probe was prepared by glueing a colloidal silica microsphere of 7.75 μm in diameter (Cospheric, USA) with a UV-curable adhesive (NOA 63, Norland Edmund Optics, Barrington, USA) to tipless NP-O10 silicon nitride cantilevers (nominal spring constant 0.1 N m^{-1}, Brucker, Billerica, USA). For the spherical probe, the indentation setpoint was 4 nN, ramp size 2 μm and probe speed 4 μm per second (testing frequency was 1 Hz). For the pyramidal probe, MLCT-E (nominal spring constant 0.1 N m^{-1}) silicon nitride cantilevers (Bruker, USA) were used, having triangular pyramid geometry (20 nm nominal radius). The operative parameters were the same but the indentation setpoint was reduced to 2 nN (to ensure indentation and not piercing). The analysis was repeated after surface functionalisation to evaluate the impact of peptide conjugation over the surface Young's modulus. Indentation data were treated with JPK software. Curves obtained from the colloidal probe were fitted between 1 and 4 nN using the Hertz model for a spherical indenter. Curves obtained from the pyramidal probe were fitted between 0.5 and 2 nN using the Sneddon correction of the Hertz model. With both probes, 8 × 8 force volume curves were collected over 20 × 20 μm regions (400 μm^2), obtaining 68 E values measured over as many surface locations. At least five regions were analysed per sample, and three different samples per condition. As previously reported,[56] E values obtained from each region were averaged to obtain one mean value, so that Young's modulus of each sample was represented by at least 5 mean values and each hydrogel condition by 15 mean values.

Surface nanotopography of DGL G5-PEG hydrogels functionalised with RGD/BMP peptides was measured in contact mode in solution. MLCT-C silicon nitride cantilevers (Bruker, USA) were used to raster-scan the surface over 400 μm^2-squared arrays to acquire 256 × 256 pixels per image. The deflection setpoint was manually adjusted to the minimum to ensure limited surface deformation while scanning. At least three different areas were imaged per sample, using three samples per condition. Height sensor images were treated using Gwyddion software, subtracting the mean plane and applying line correction. To calculate surface roughness, Gwyddion software was used to extract the surface root-mean-square roughness (RMS).

Hydrogel functionalisation with GRGDSPC and BMP-2 peptides

The GRGDSPC and the BMP-2 peptides were conjugated to hydrogel surfaces using the heterobifunctional Mal-PEG-NHS ester spacer (see Fig. S10, ESI†). In a 48-well plate, 200 μL of a 5 mM solution in phosphate monobasic buffer (0.01 M, pH 7.3) were added to cover the hydrogel surface and allowed to react for 1 h at room temperature under gentle agitation. A 10-fold molar excess of crosslinker to peptide was used (1 μmol per 0.1 μmols of peptides). The peptides were separately dissolved in DMSO at 10^{-2} M and diluted to 5×10^{-4} M (0.5 mM) with water. The two peptide solutions were mixed in equimolar amounts and 200 μL of the final solution were added to the activated hydrogels, allowing the coupling to run for an hour under gentile agitation. Then, the functionalised hydrogels were transferred to 50 mL-Falcon tubes and rinsed in PBS to wash away all non-grafted peptides, changing the rinsing solution once a day, until no colouration occurred.

Estimation of surface-grafted peptide densities

A Zeiss Axio Observer inverted confocal microscope (Zeiss, Germany) was used to measure the density of grafted peptides at the surface using a 10× objective with 0.45 numerical aperture (NA). Three locations per gel were selected, by focusing on the first surface plane and collecting a Z-stack of 5 μm-apart slices (over 50 or 200 μm) at 1024 × 1024 pixels (1278 × 1278 μm, 1.25 μm per pixel). Laser excitation power was 0.03%, excitation wavelength 561 nm and detection range of emitted light 565–605 nm, with 1 Airy unit pinhole size. The optical section of the Z-slicing was therefore calculated as 4.49 μm, full width at half maximum (FWHM), according to the following equation:

$$\text{Axial resolution (FWHM)} = \frac{0.88\lambda_{\text{exc}}}{\left(n - \sqrt{n^2 - \text{NA}^2}\right)} \tag{3}$$

Where excitation wavelength (λ_{exc}) was 561 nm, the refraction index (n) of the air was 1 and the numerical aperture (NA) of the objective was 0.45. Surface peptide densities were obtained by measuring the intensity of the most intense slice of each Z stack and dividing the raw integrated density values measured by 4, to have a density estimation over a 1 μm-thick surface section. Fluorescence intensity values were converted into peptide densities of pmols mm^{-2} $(\mu m)^{-1}$ using calibration curves acquired with the same settings, by placing 0.8 μL drops of fluorescent peptide solutions over a silanised glass slide. A Z-stack was collected per drop and fluorescence intensity was calculated in the most intense slice (calibrations curves are available in Fig. S12, ESI†). Images were analyzed using ImageJ freeware.

Indirect cytotoxicity of DGL G5-PEG hydrogels

Indirect cytotoxicity tests were performed to verify the potential leaching of dendrigraft nanoparticles from crosslinked hydrogels. Following the ISO-1993-12, the extracts obtained from non-functionalised DGL G5-PEG hydrogels (according to ISO-10993-12:2004) were tested on the same hMSCs line used for cell culture experiments. Hydrogels were sterilised overnight in 70% v/v aqueous ethanol, then rinsed for a day in PBS and equilibrated in DMEM before testing. In a plastic Falcon tube capped, 3 gels per condition were extracted with 3 mL of DMEM + 10% FBS (1.25 cm^2 mL^{-1} extraction ratio, having materials >1 mm thick) for 24 h under agitation in a humidified chamber at 37 °C and 5% CO_2. Sterilised glass coverslips were used as negative test materials. The positive control was DMSO 10% in DMEM and the reference for cell viability was DMEM + 10% FBS (normal medium). hMSCs (passage 4) were subcultured once before seeding in a 96-well plate at subconfluent densities. The day after, the extraction medium (150 μL) was added to 6 replicate wells per condition (testing materials and controls). Cells were left in contact with the extracts for 24 h in a humidified chamber at 37 °C and 5% CO_2. Then, 50 μL of extraction medium were replaced with the same volume of the XTT solution. After 4 h, the optical density (O.D.) was measured with a plate reader at 490 nm, subtracting the reading at 690 nm (reference wavelength). Three readings per well were acquired, for 6 wells per condition. The mean cell viability is reported in percentage (%) of the reference viability in a normal medium (100%).

Cell culture experiments

hMSCs at passage 4 (P4) were thawed two days before seeding and subcultured in a growth medium at 37 °C with 5% CO_2. Hydrogels were sterilised overnight in 70% v/v aqueous ethanol, then rinsed for a day in PBS and equilibrated in DMEM before cell seeding. To avoid floating, the hydrogel discs were carefully fixed with a sterile agarose solution to the bottom of 24-well plates. For the study of cell adhesion, hMSCs (at P5) were seeded on the hydrogel surfaces and glass coverslips (controls) at a density of 2000 cells per cm^2 in DMEM (without Phenol Red) + 1% penicillin/streptomycin, adding 10% FBS only to glass controls. After 6 h, cells were fixed in aqueous paraformaldehyde at 4% for 15 minutes at 4 °C, washed thoroughly and stored in PBS at 4 °C. For cell differentiation studies, hMSCs (at P5) were then seeded on the hydrogel surfaces and glass coverslips (controls) at a density of 2000 cells per cm^2 in DMEM (without Phenol Red) +1% penicillin/streptomycin, without serum for the first 4 h of culture (0.9 mL). Then, the culture medium was supplemented with 0.1 mL FBS (10% final concentration). 24 h after seeding, the culture medium was replaced with the osteogenic differentiation medium, changed twice a week. After 14 days of culture, cells were fixed in aqueous paraformaldehyde at 4% for 15 minutes at 4 °C, washed thoroughly and stored in PBS at 4 °C.

Quantification of hMSC adhesion and osteogenic differentiation

After fixing and washing to remove PFA traces, cells were permeabilised with 0.3% Triton X-100 in PBS for 5 min at 4 °C, then incubated in 1% bovine serum albumin (BSA) in PBS for 1 h at 37 °C to saturate non-specific adsorption sites. For the cell adhesion study, focal complexes were visualised *via* vinculin immunofluorescence staining. 200 µL of the primary antibody (mouse) were added to each hydrogel sample, at a 1 : 200 dilution in PBS/BSA 1% solution, and incubated for 1 h at 37 °C. After rinsing in PBS, 200 µL of the secondary antibody Alexa Fluor 568 (rabbit anti-mouse) were added, at a 1/400 dilution in PBS/BSA 1% solution, and incubated for 1 h at 37 °C. For the cell differentiation study, the osteogenic marker Osteopontin was quantified *via* immunofluorescence staining. 200 µL of the primary antibody (mouse) were added at a 1 : 200 dilution in 1% BSA/PBS and incubated for 1 h at 37 °C. After washing in PBS, 200 µL of the secondary antibody AlexaFluor647 (goat anti-mouse) were added at 1 : 400 dilution in 1% BSA/PBS and incubated for 1 h at 37 °C. Cell morphology and cytoskeletal architecture were visualised by labelling filamentous actin (F-actin) with Alexa Fluor 488 (1 : 40 dilution) for 30 minutes at 37 °C. Cell nuclei were stained using DAPI at 1 µg mL^{-1} (1 : 1000 dilution) in UP water for ten minutes at r.t. Then, cells were imaged with a Leica DM5500B epifluorescence microscope (Leica Biosystems, Germany). Images were analyzed using ImageJ freeware. Cell morphology in the adhesion and differentiation studies was analysed at 40× magnification, measuring the spread area and aspect ratio (AR) with ImageJ software in at least 30 cells per sample. AR (defined as the ratio of major cell axis/minor cell axis) was measured in ImageJ by outlining cell profiles in fluorescence images. Cell densities after two weeks of cultures were assessed by counting the number of cells (nuclei) per field of view on images taken with a 10× objective (900 × 700 µm field of view), on at least 24 different images. Osteopontin (OPN) nuclear expression was quantified at 40× magnification, by calculating the raw integrated density in the nucleus (selected using the wand tool) after background subtraction. For OPN quantification, between 300 and 600 cells were analysed in total, seeded in two hydrogel samples per condition, for two independent experiments ($N = 2$).

Statistical analysis

Statistical significance was analysed in GraphPad Prism software 8.0.1 for Windows (GraphPad Software Inc., La Jolla, CA, USA). Shapiro-Wilk tests were used to determine the normality of data distributions. Normally distributed data were analysed using one-way ANOVA *post hoc* Tukey's multiple comparison tests. Non-normally distributed data were analysed using the non-parametric Kruskal–Wallis test with Dunn's correction for multiple comparisons. The statistical test used is reported in the caption under each graph. Differences were considered significant for p-value < 0.05 (two-sided), and represented as follows: $P < 0.05$ (*), $P < 0.01$ (**), $P < 0.001$ (***).

Results and discussion

Synthesis and physical characterisation of DGL G5-PEG hydrogels

DGL G5-PEG hydrogels were synthesised by end-linking of the amine end-groups on DGL G5 macromolecules (schematised in Fig. 1(a)) with the terminal carboxylic groups of commercially available, difunctionalised PEG chains (dicarboxylic acid-PEG in Fig. 1(a)). The network's crosslinking density of amide bonds was modulated by varying the concentration and stoichiometry of the two reactants. For the following experiments, four conditions were selected, named 65 mM-3, 50 mM-5, 65 mM-4 and 65 mM-5. Because of the multivalency of DGL G5 molecules, the formation of inter-macromolecular bonds between DGL G5 and dicarboxylic-acid PEG chains (effective network crosslinks, shown in green in Fig. 1(b)) competes with the formation of intra-molecular loops on a DGL G5 molecule (surface crosslinks, in orange in Fig. 1(b)), which is favoured by the limited mobility of PEG chains attached at one end.[52,57] The formation of these topological defects was observed, for the first time, for PAMAM dendrimers crosslinking epoxy-terminated PEG chains[47] and reported, more recently, also for DGL G3 reacting with NHS-functionalised PEG chains.[49] Consequently, increasing the PEG concentration only allows the formation of more bonds without shifting the equilibrium towards one specific product. Conversely, we expected that increasing the dendrigraft molar fraction (ranging here from

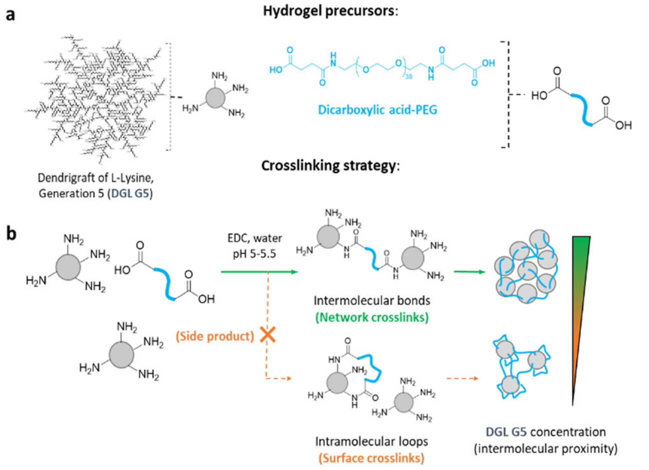

Fig. 1 Synthetic strategy of DGL G5-PEG hydrogels. (a) Schematic representation of hydrogel precursors, DGL G5 dendrigrafts and dicarboxylic acid-PEG polymers. (b) Crosslinking reaction based on intermolecular amide bonds (network crosslinks) formation between the DGL G5 nanoparticles. Increasing DGL G5 concentration (intermolecular proximity) in the hydrogel precursor solution favours the formation of intermolecular amide bonds (network crosslinks).

0.42 to 0.92 mM) for a fixed PEG concentration (which means a fixed number of network crosslinks possibly available), would increase the DGL G5 intermolecular proximity, thereby promoting intermolecular crosslinks formation.[52] First, we verified the formation of an amide bond network in crosslinked hydrogels. Collectively, the infrared spectra of lyophilised hydrogels (reported in Fig. S1, ESI†) show symmetric signals, indicating high bond structure similarity. The quantitative reaction of carboxylic groups is confirmed by the absence of COOH signals in the spectra of 65 mM-3 and 50 mM-5 gels, whereas 65 mM-4 and 65 mM-5 gels show only a small shoulder peak at 1730 cm^{-1} (COOH stretching). As these two last hydrogels are stiffer, one can assume that the crosslinking speed reduces the probability of interactions between carboxylic and amine groups, thus reducing the yield of bond formation during hydrogel synthesis. To further confirm the validity of our strategy, we used shear rheometry measurements to characterise hydrogel crosslinking and rapidly screen the mechanical properties before swelling. *In situ* prepared hydrogels crosslinked within twelve minutes after EDC addition at room temperature (see Fig. S2 and S3, ESI† for detailed characterisation of selected DGL G5-PEG conditions before swelling). As shown in Fig. 2(a), the storage modulus (G') increased linearly with the DGL-G5 crosslinker concentration. This trend indicates a more rapid increase in hydrogel stiffness at the higher dicarboxylic acid–PEG concentration (65 mM). Increasing the PEG concentration from 50 to 65 mM led to slightly stiffer gels (46.33 ± 3.28 and 66.73 ± 0.90 kPa for 50 mM-5 and 65 mM-4 gels, respectively) while doubling the DGL-G5 concentration (from 0.42 to 0.85 mM) led to an almost 8-fold increase in G' (9.54 ± 1.69 and 79.17 ± 4.42 kPa for 50 mM-3 and 50 mM-6, respectively). Consistent with previous reports on DGL G3,[52] the stiffness of DGL G5-PEG hydrogels depended on the total molecular composition but was primarily dominated by the concentration of the DGL-G5 crosslinker. Swelling measurements also confirm these observations, showing a decrease in the fluid absorption capacity (FAC) with increasing DGL-G5 concentration, which indicates the formation of more densely crosslinked polymer networks (available in Fig. S4A and B, ESI†).[23]

Macroscale mechanical characterisation of DGL G5-PEG hydrogels

The dynamic, viscoelastic behaviour of DGL G5-PEG hydrogels was initially characterised by rheological measurements after equilibrium swelling. Network expansion due to increased water content after swelling significantly diminished the (shear) storage modulus (G') but did not change the overall stiffness gradient. Collectively, G' decreased by 6 to 10 times after swelling, possibly due to the higher conformational mobility (and thus lower resistance to deformation and internal friction) of the polymer chains in the swollen state, consistent with the entropic origin of rubberlike elasticity.[58,59]

Fig. 2(b) shows that the G' of swollen gels was 2.9 ± 0.3 kPa for 65 mM-3, 4.5 ± 0.6 kPa for 50 mM-5, 7.6 ± 0.9 kPa for 65 mM-4 and 10.0 ± 0.9 kPa for 65 mM-5. The storage modulus was linear and frequency-independent in the 0.01–16 Hz range, similar to what was observed before swelling. The loss modulus (G''), around two orders of magnitude lower than G', displayed a slight increase at high frequencies, more visible in the softer samples. As the G'' describes the viscous component of the hydrogel's viscoelastic behaviour, the slow response of polymer network at faster deformation rates results in the uncomplete relaxation of the chains, that can lead to a higher loss modulus.[60] Collectively, G'' values ranged between 100 and 200 Pa and, consistently with the higher water content, showed an increase from the pre-swelling values (comprised between 10 and 100 Pa, Fig. S2 and S3, ESI†). Accordingly, the loss factor ($\tan\delta$, G''/G'), representative of the hydrogel viscoelastic character, was close to 0.01 for all samples tested (data not shown).[61] Collectively, these results showed that DGL G5-PEG hydrogels have a predominantly elastic behaviour in the frequency range tested, which is consistent with their covalent bond structure.[62] The gels were also analysed in compression tests to explore whether hydrogels' stiffness measurements at the macroscale are influenced by the deformation mode applied. The macroscale Young's modulus (calculated from stress–strain curves at 5% deformation, illustrated in Fig. S5, ESI†) was 8,8 ± 1,1 kPa for 65 mM-3, 13,1 ± 1,0 kPa for 50 mM-5, 19,0 ± 0,5 kPa for 65 mM-4 and 25,1 ± 3,1 kPa for 65 mM-5, as shown in Fig. 2(c).

The hydrogel's shear complex modulus (G^*) can be correlated to Young's modulus by knowing the material's Poisson's ratio (ν) according to the following equation: $E = 2G'(1 + \nu)$ (eqn (2)). Hence, approximating $G^* \approx G'$ (as G'' is negligible for the selected DGL G5-PEG hydrogels),[56,63] the Poisson's ratio of these gels was calculated as 0,52 for 65 mM-3, 0,46 for 50 mM-5, 0,26 for 65 mM-4 and 0,26 for 65 mM-5, as illustrated in Fig. 2(c). Interestingly, these results show that the hydrogels with the lower polymer volume fraction, 65 mM-3 and 50 mM-5,

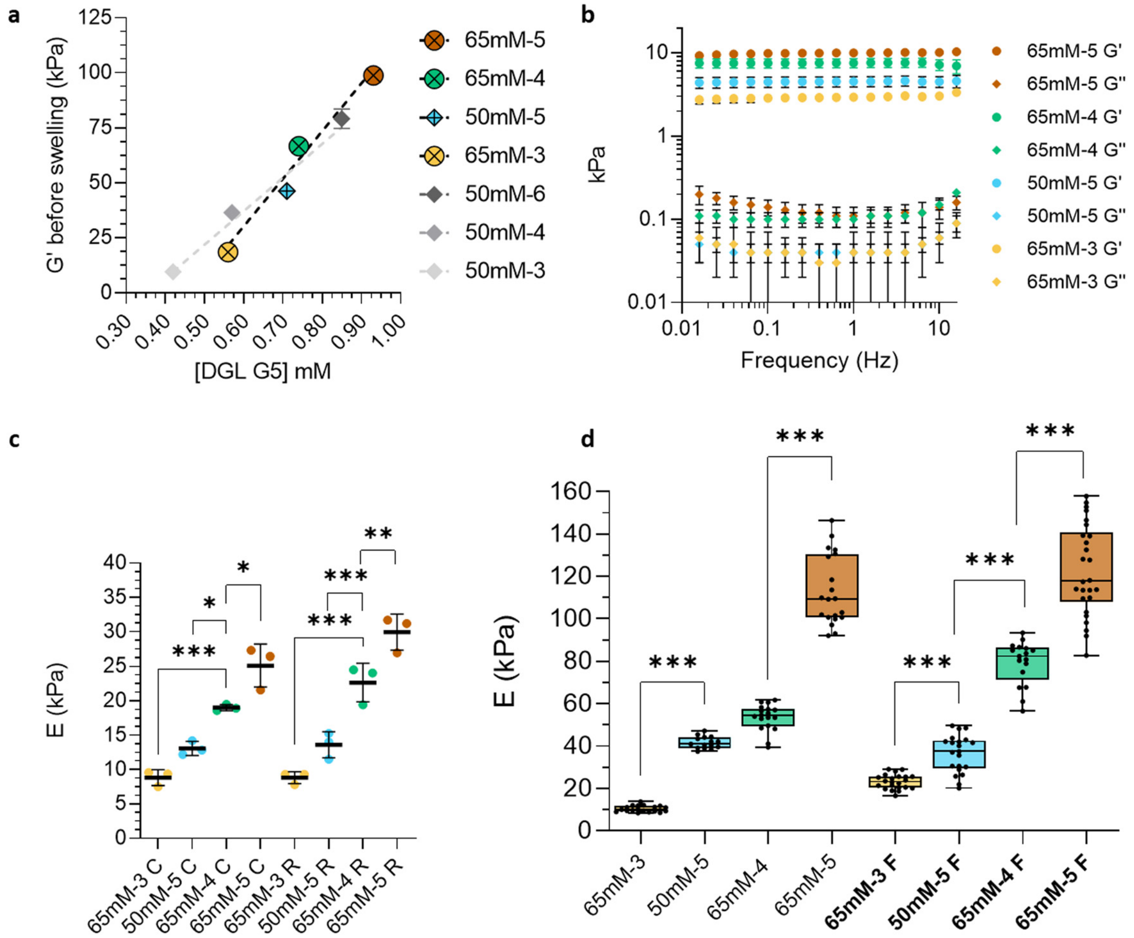

Fig. 2 Multiscale mechanical characterisation of DGL G5-PEG hydrogels. (a) Linear correlation between hydrogel stiffness (G' before swelling, kPa) and DGL G5 crosslinker concentration (mM), with a steeper increase (slope of the fitting line, m) for 65 mM PEG concentration (R^2 values are 0.956 for 50 mM and 0.979 for 65 mM conditions). (b) Rheometry measurements: 0.01–15 Hz frequency sweeps showing the G' (circles) and G'' (diamonds) after swelling. (c) Inter-group comparison of E values (kPa) calculated from compression (c) and rheometry (R) data, using the $E = 3G'$ ratio. $N = 3$, one-way ANOVA (Tukey's correction for multiple comparisons) with $P < 0.05$ (*), $P < 0.01$ (**), $P < 0.001$ (***). (d) AFM measurements: E values (kPa) at the surface nanoscale measured with a pyramidal tip before (left group) and after peptide functionalisation (F, in bold characters, right group). Each point represents the averaged E value over a squared array of 400 μm^2 (20 × 20). At least five different regions were analysed per gel. N (gels) = 3, one-way ANOVA (Tukey's correction for multiple comparisons) with $P < 0.05$ (*), $P < 0.01$ (**), $P < 0.001$ (***). Not significant = $P > 0.05$. All statistical tests are reported in the ESI.†

are very close to the theoretical value of 0,5 and, thus, can be assumed as incompressible networks. However, as the polymer volume fraction increases for 65 mM-4 and 65 mM-5 gels, the Poisson's ratio decreases to 0.26, indicating that these more densely crosslinked gels lose volume when compressed. Overall, E/G' ratios ranged from 3,0 (65 mM-3) to 2,9 (50 mM-5) to 2,5 (65 mM-4 and 65 mM-5). When DGL G5-PEG hydrogels' elastic behaviour was approximated to that of rubber-like materials (ν equal to 0.5), E calculations based on rheometrical data were 8.8 ± 0.90 kPa for 65 mM-3, 13.6 ± 1.9 kPa for 50 mM-5, 22.7 ± 2.8 for 65 mM-4 and 29.9 ± 2.6 for 65 mM-5 (illustrated in Fig. 2(c)). Statistical testing found no significant differences in paired E values calculated from macroscale measurements in compression or shear rheometry. Therefore, even though DGL G5-PEG hydrogels diverge from the theoretical value of 0,5 at high DGL G5 crosslinker concentrations (>0,54 mM), the assumption that they behave as incompressible networks is still valid, as the approximation of $E \sim 3G'$.[64,65] Considering inter-group comparisons, 65 mM-3 and 50 mM-5 gels showed no statistically different stiffness in compression (E values) and oscillatory rheometry (G' values) measurements. To find any stiffness differences at the surface micro- and nanoscale, the selected DGL G5-PEG hydrogels were also analysed in atomic force microscopy (AFM).

Surface mechanical characterisation of DGL G5-PEG hydrogels

AFM nanoindentation[66] with colloidal and pyramidal tips was used to compare the influence of surface measurements and indentation geometry on Young's modulus calculations. Moreover, the hydrogels were also analysed after surface functionalization using the pyramidal probe to evaluate if peptide grafting impacted surface stiffness. E values (mean ± SD) extracted from indentations with the colloidal tip were 10.5 ± 5.2 kPa for 65 mM-3, 27.9 ± 3.5 kPa for 50 mM-5, 52.8 ± 8.8 kPa for 65 mM-4 and 77.7 ± 13.6 kPa for 65 mM-5 kPa (Fig. S6, ESI†). *E* values (mean ± SD) calculated from indentations with the pyramidal tip were 10,4 ± 1,5 kPa for 65 mM-3, 41.7 ± 2.8 kPa for 50 mM-5, 53.6 ± 6.2 for 65 mM-4 and 113.0 ± 16.5 kPa for 65 mM-5. When looking at inter-group comparisons, the colloidal tip showed no significant differences in stiffness among nearby groups, reporting statistically different *E* values ($P < 0.001$) only for 65 mM-3 and 65 mM-4 gels, 65 mM-3 and 65 mM-5 gels and 50 mM-5 and 65 mM-5 gels (Fig. S6, ESI†). Instead, when measured with the pyramidal tip, *E* values were statistically different among nearby groups, except for 50 mM-5 and 65 mM-4 (Fig. 2(d)). Collectively, Young's modulus values extracted from AFM force curves were higher than those measured at the macroscale from compressive and shear deformations. Although statistical testing showed no significant differences among *E* values obtained with the two probes, the pyramidal tip afforded higher values than the colloidal one at the highest crosslinker concentration (65 mM-5 gels), similar to previous reports.[56] This overestimation, observed particularly when indenting the surface with a pyramidal tip, is a well-known effect of AFM-based *E* measurements and was described, in the literature, with even greater discrepancies than those observed here.[56,63,67] Apart from the inherently anisotropic behaviour of materials at the interface[7,68] and nanoscale surface heterogeneities – both of which are known to affect surface measurements – the effect of the tip geometry is possibly due to a non-linearly elastic deformation of polymeric networks when high local stresses are applied, as with sharp pyramidal tips. Consequently, if the contact area between the probe and the surface changes during the indentation, the fitting models might underestimate this effect and yield higher *E* values.[56,64,65,69] In contrast, colloidal tips with spherical geometry induce larger surface deformations, having more predictable contact areas (but lower lateral resolution) and limiting this overestimation effect. As compared to *E* values measured in compression and rheometry tests, these results show that the correlation observed at the macroscale between hydrogel stiffness and DGL G5 concentration is also valid for surface measurements in AFM. However, considering that AFM results are consistently higher, the E/G' ratios deviated from the previously observed ratio of 3, which was found valid only for 65 mM-3 gels (3,6). More concentrated hydrogels afforded substantially higher ratios, comprised between 6.8–7.1 (65 mM-5 and 65 mM-4, respectively) and 9,3 (50 mM-5), as already reported for PEG-maleimide gels crosslinked by thiol-containing peptides.[63] After bioactive functionalisation, the surface *E* values (mean ± SD) of DGL G5-PEG hydrogels were as follows: 23.2 ± 3.5 kPa for 65 mM-3 (an increase of 12.8 kPa compared to pre-functionalization), 34.9 ± 9.2 kPa for 50 mM-5 (a decrease of 6.8 kPa), 79.3 ± 10.3 kPa for 65 mM-4 (increase of 25.7 kPa), and 123.0 ± 21.3 kPa for 65 mM-5 (increase of 10 kPa), as illustrated in Fig. 2(d) (right group, in bold characters). While surface functionalisation generally increased *E* values, this effect was particularly pronounced for 65 mM-4, with smaller changes for 65 mM-3 and no statistical significance for other conditions (as reported in Fig. S7, ESI†). Moreover, statistical testing of hydrogel stiffness after functionalisation showed significant differences among all the groups. Few previous studies have explored the impact of surface functionalisation on hydrogel stiffness using AFM, reporting contradictory findings.[32,70] For example, recent work from Durrieu's group[32] found that grafting the same BMP-2-derived peptide used here onto PA hydrogels through sulfo-SANPAH led to no significant variations of surface *E* values measured in AFM. Contrasting with the results, Lanniel and coworkers[70] previously demonstrated that different surface coatings significantly altered PA hydrogel stiffness. Our findings seem to align with the latter, suggesting that surface functionalisation can modify hydrogel stiffness. Additionally, topographical mapping in contact mode (in Fig. S9, ESI†) using the pyramidal tip confirmed that surface roughness did not change across the four hydrogels after functionalisation, indicating that the observed stiffening is unlikely to be caused by peptide aggregates. Surface topographical features, calculated as the root mean square roughness (RMS), ranged between 8 and 13 nm (Fig. S9, ESI†), consistent with previous data for PEG gels.[56]

These data confirm that varying the networks' crosslinking degree to modify the hydrogels' stiffness did not result in different surface topographies, which could have affected the behaviour of cells adhering on top.

Surface functionalisation with GRGDSPC and BMP-2 biomimetic peptides

Lacking integrin-binding motifs, native DGL G5-PEG hydrogels require surface functionalisation with adhesive ligands to support cell attachment and growth.[24] In this work, the hydrogel surfaces were functionalised with equimolar concentrations of a GRGDSPC adhesive sequence and a BMP-2 biomimetic peptide (bp), an osteoinductive factor developed by our group, to favour hMSCs differentiation.[17] These peptides are known to elicit synergic effects when co-grafted on material surfaces.[35] The peptides were covalently immobilised to avoid their potential release and enable their density quantification. Grafting was achieved using a bifunctional PEG spacing chain bearing a maleimide group at one end and an NHS ester at the other (Mal-PEG-NHS spacer, Fig. S10C, ESI†). For peptide coupling, the spacer reacts by the NHS ester group with the primary amines available in DGL G5, left unreacted after hydrogel crosslinking (Fig. S10, ESI† step 1). After tethering the spacer to hydrogel surfaces, cysteine-containing peptides are coupled through the Michael addition of thiol groups to the maleimide moiety (Fig. S10, ESI† step 2). This strategy allowed the controlled coupling of one peptide to a single PEG spacer selectively at the C-terminal cysteine (Fig. S10, ESI† step 3). Therefore, it is more advantageous than widespread conjugation methods using, for example, sulfo-SANPAH,[71–73] which can result in peptide presentation in an inactive form. Surface grating densities were estimated *via* confocal microscopy using fluorescent (TAMRA-conjugated) peptides. Fig. 3 reports the

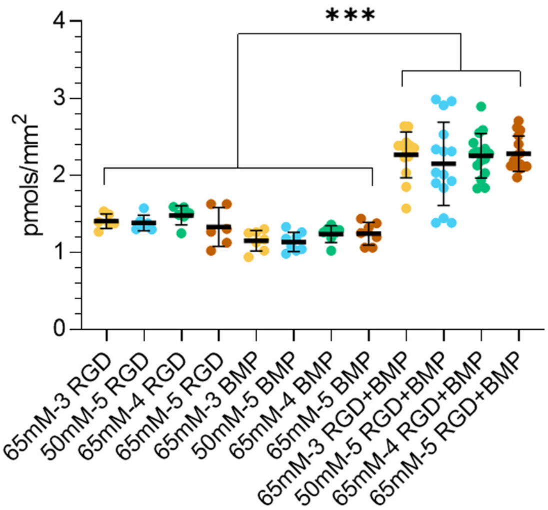

Fig. 3 Evaluation of fluorescent peptide grafting density to hydrogel surfaces. All hydrogels are functionalised with the same equimolar peptide combinations. To quantify the relative density of GRGDSPC (RGD) and BMP-2 bp (BMP), the hydrogels were functionalised adding one fluorescent peptide in the equimolar mixture (RGD in the left group and BMP in the middle group) or both fluorescent peptides (RGD + BMP, right group). Each point represents one measurement over a "surface" area of 1278 × 1278 μm^2 (1 μm-thick). Bars express mean ± SD of all surface measurements. N (gels) $\geq$ 3, one-way ANOVA (Tukey's correction for multiple comparisons) with $P < 0.05$ (*), $P < 0.01$ (**), $P < 0.001$ (***). Not significant = $P > 0.05$. All statistical tests are reported in the ESI.†

confocal estimations of peptide grafting densities calculated over approximately 1 μm, which can be considered a "surface" density.

Overall, "individual" grafting densities of GRGDSPC and BMP-2 bp showed no statistically significant differences within their groups or between the two groups, even though the relative density of GRGDSPC peptide grafting was slightly higher. The average grafting density of GRGDSPC peptides was 1.4 + 0.2 pmols mm^{-2} (RGD group, left in Fig. 3) while the BMP-2 one was calculated as 1.2 + 0.1 pmols mm^{-2} (BMP group, middle in Fig. 3). As expected, the fluorescence intensity increased when the two peptides in the mixture were fluorescent, confirming the surface co-grafting of both peptides. The total peptide concentration (RGD + BMP group, right in Fig. 3) ranged from 2.2 ± 0.5 (between 1,0 and 1,6 peptides nm^{-2}) to 2,3 ± 0,2 pmols mm^{-2} (between 1,2 and 1,5 peptides nm^{-2}), with an average grafting density of 2.2 ± 0.4 pmols mm^{-2}, which well correlates with the estimations of relative peptide density. *Z*-Axis profiling showed a concentration gradient for the first tens of μm from the surface, over approximately 50 μm for GRGDSPC peptides and 150 μm for the BMP-2 bp (an example of a 3D reconstruction obtained in confocal microscopy Z-stacks is reported in Fig. S11, ESI†). The peptide densities found on DGL G5-PEG hydrogels are consistent with recent works on various functionalised surfaces,[74] including hydrogels.[27,32] The literature shows that co-grafting RGD-containing peptides and BMP-2 proteins[33] or mimetic peptides[27] on hydrogel surfaces, as we did, improves cell adhesion and reduces the concentrations of individual peptides required for osteoinduction.[34,75] Zouani and collaborators showed an upregulation of osteogenic markers in pre-osteoblast cells already at 0.7 pmol mm^{-2} of GRGDSPC and 1.0 pmol mm^{-2} of the BMP-2 bp used here,[28] suggesting that the grafting densities reported here are sufficient to allow hMSC adhesion and advance their osteogenic commitment. Moreover, these results prove that DGL G5 can be incorporated into hydrogels to enable surface functionalisation with high densities of Cys-containing peptides, that can be selectively grafted at the C-terminus using maleimide chemistry.

Cytotoxicity of DGL G5 leaching from crosslinked hydrogels

DGL G5-PEG hydrogels were initially tested with an *in vitro* indirect cytotoxicity assay to exclude the potential release of cytotoxic DGL G5 molecules from the hydrogels. Uncrosslinked DGLs, like other amine-terminated macromolecules, exhibit highly polycationic surfaces at physiological pH (due to free amine protonation), causing cell membrane disruption and inducing concentration-dependent cytotoxic effects.[42,43] Exposure to the extracts for 24 h did not reduce hMSCs metabolic activity, thus proving that DGL G5 can be safely incorporated as hydrogel crosslinkers (see Fig. S13, ESI†).

Evaluation of early hMSC adhesion and spreading

In a preliminary study to evaluate the impact of functionalised DGL G5-PEG hydrogels on early cell adhesion, hMSCs were cultured onto hydrogel surfaces in media without serum and fixed 6 h after seeding. As visible in the top raw images in Fig. 4(a), the highest number of cells per field of view was observed on control glass surfaces in the presence of serum. Conversely, less cells adhered to all the other hydrogel conditions after 6 h in serum-less media, with the lowest cell number observed on the softest hydrogels (65 mM-3). Cell morphology and spreading were also altered by hydrogel stiffness after 6 h. On 65 mM-3 gels, cells exhibited spherical morphology and the lowest spreading area (around 450 μm^2) and aspect ratio, similar to recent observations on soft PAAM hydrogels with a short ligand spacing at 24 h (Fig. 4(b) and (c)).[13] As shown in Fig. 4(b), cell area increased nearly five-fold on 50 mM-5, 65 mM-4 and 65 mM-5 hydrogels compared to 65 mM-3, reaching a plateau around 2200 μm^2 on these three conditions (with no significant differences, as reported in Table S6, ESI†) and exhibiting greater spreading than on glass controls (approximately 1400 μm^2). Conversely, while cell area remained unchanged across these three conditions, the cell aspect ratio (as shown in Fig. 4(c)) peaked on 50 mM-5 gels after 6 h and then decreased on 65 mM-4 and 65 mM-5. This suggests that once maximum spreading is achieved at a specific substrate stiffness, cell traction forces alter the cell's shape to more polygonal morphologies, similar to previous observations on substrates with comparable stiffness.[76] Looking at the cytoskeletal organisation and the formation of adhesion complexes, phalloidin staining revealed highly anisotropic F-actin distributions and no clear localisation of the integrin-associated protein vinculin on 65 mM-3 gels. On glass controls, cells showed

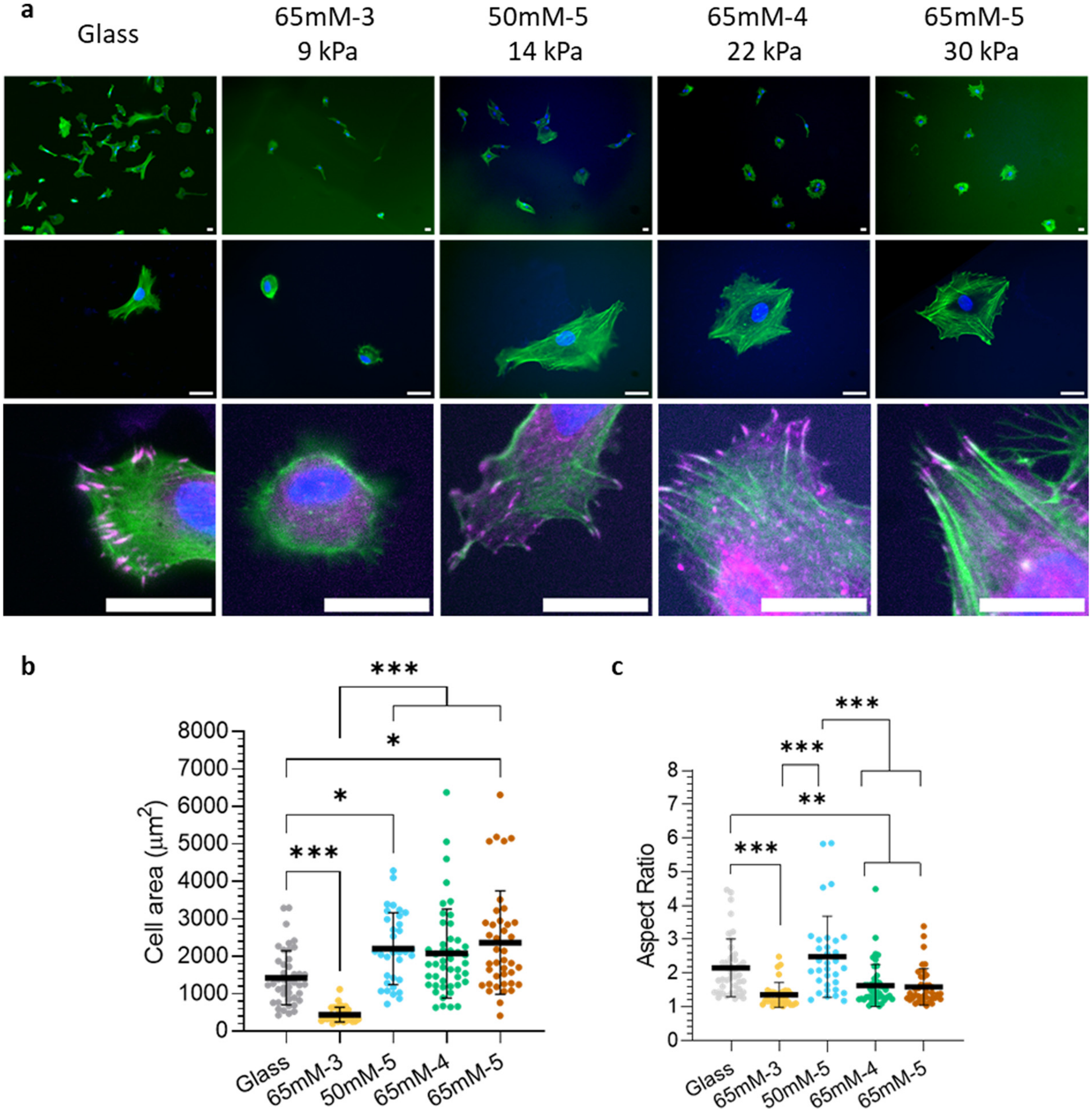

Fig. 4 hMSC adhere and spread on functionalised DGL G5-PEG hydrogels after 6 h without serum. (a) hMSCs cultured for 6 h in a normal medium (DMEM without Red Phenol), adding 10% serum to glass controls. Fixed cells were stained for vinculin in magenta (anti-vinculin antibody), F-actin in green (phalloidin) and nuclei in blue (DAPI), with 10× (top) or 40× objectives (middle and bottom). The bottom line shows magnified images of the cell lamellipodial edge, where nascent adhesion complexes are visible. Scale bar 25 microns. (b) hMSC spreading area (measured for isolated cells) after 6 h of culture, depicted as mean ± 1 SD. (c) Aspect ratio (calculated as the length ratio of the longest and shortest cell axis of isolated cells) of hMSCs after 6 h of culture, depicted as mean ± 1 SD. *N* (gels) = 2, non-parametric Kruskal–Wallis test with Dunn's correction for multiple comparisons, with $P < 0.05$ (*), $P < 0.01$ (**), $P < 0.001$ (***). Not significant = $P > 0.05$. All statistical tests are reported in the ESI.†

elongated morphologies and vinculin staining (in magenta in the bottom raw of magnified images, Fig. 4(a)) revealed the formation of nascent focal adhesion at the cell's edge, mostly oriented towards the cell nucleus. However, F-actin staining does not evidence the clear assembly of stress fibres at this time point, contrary to cells on 50 mM-5, 65 mM-4 and 65 mM-5 gels, which exhibited visible and aligned stress fibres connected to the membrane adhesion complexes. These results suggest that, without serum addition, hMSCs could adhere and spread on DGL G5-PEG hydrogels functionalised with GRGDSPC and BMP-2 bp and developed more organised stress fibres on 50 mM-5, 65 mM-4 and 65 mM-5 gels than on glass controls in the presence of serum.

Evaluation of late hMSC morphology and osteogenic commitment

To evaluate the biological activity of DGL G5-PEG hydrogels at a longer time point, hMSC morphology and osteogenic

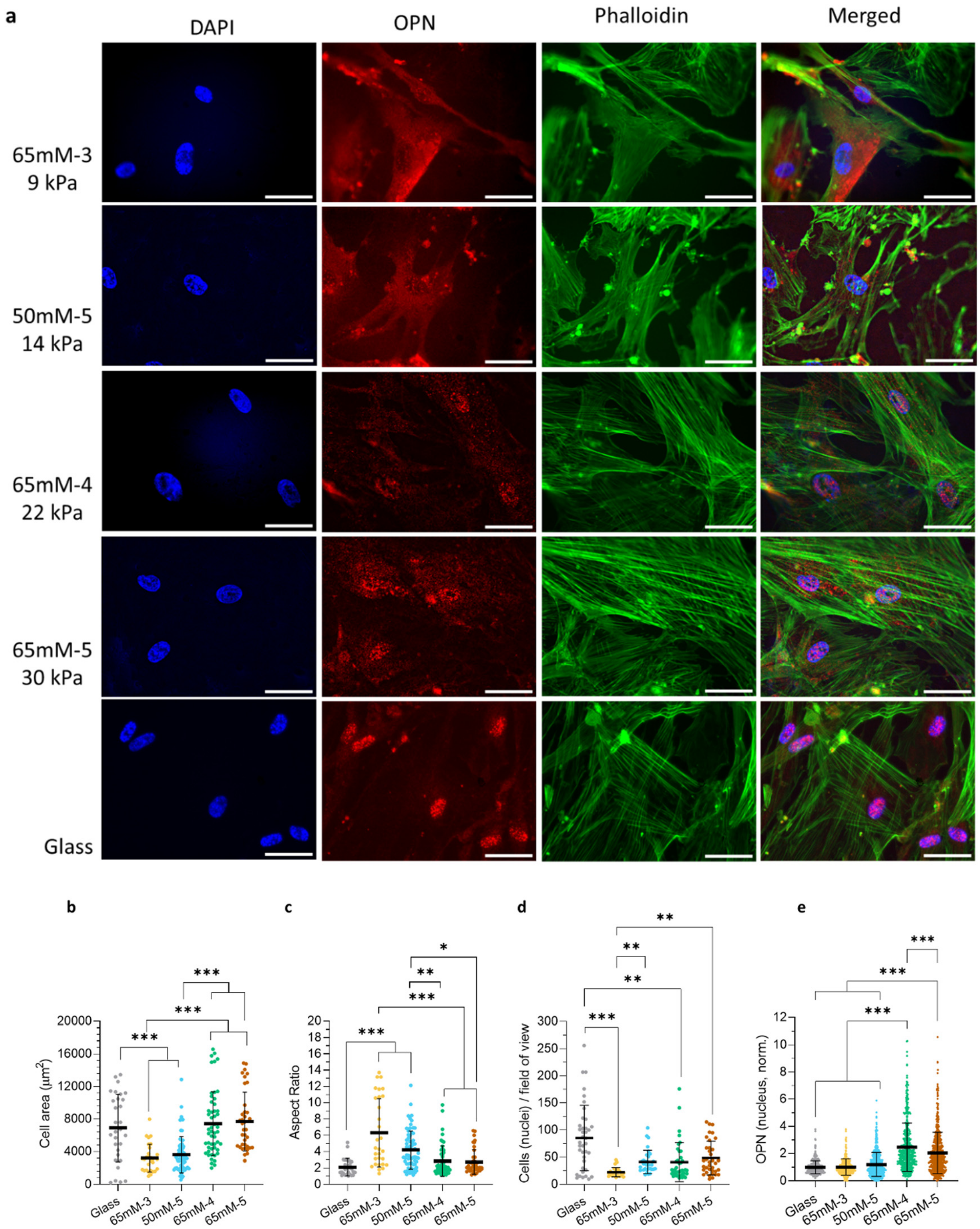

Fig. 5 hMSC spreading and differentiation after two weeks in osteogenic media. (a) hMSCs cultured on selected DGL G5-PEG hydrogels and controls were stained for nuclei in blue (DAPI column, left), osteopontin in red (OPN column, middle-left) and F-actin in green (phalloidin column, middle-right group). The right group shows the merged channels (merged column, left group). Images were taken at 40× magnifications. Scale bar 50 microns. (b) hMSC spreading area (measured for isolated cells) after two weeks of culture in OM, depicted as mean ± 1 SD. Each dot represents one cell measurement. *N* (gels) = 2. (c) aspect ratio of hMSCs after two weeks of culture in OM, depicted as mean ± 1 SD. Each dot represents one cell measurement. *N* (gels) = 2. (d) Estimated cell densities after two weeks of culture, calculated by counting the number of cells (nuclei) per field of view (900 × 670 microns at 10× magnification) using ImageJ. Each dot represents the count of one field of view. *N* (gels) ≥ 4, *N* (experiments) = 2. (e): osteopontin (OPN) expression levels measured in the cell nucleus after two weeks of culture in OM, depicted as mean ± 1 SD. Each dot represents one cell measurement. *N* (gels) = 4, *N* (experiments) = 2. Non-parametric Kruskal–Wallis test with Dunn's correction for multiple comparisons, with $P < 0.05$ (*), $P < 0.01$ (**), $P < 0.001$ (***). Not significant = $P > 0.05$. All statistical tests are reported in the ESI.†

commitment were analysed after two weeks of culture in osteogenic media (Fig. 5(a)). The measured cell area ranged from 4000 μm^2 on 65 mM-3 (9 kPa in compression) and 50 mM-5 (14 kPa in compression) hydrogels to more than 7000 μm^2 on 65 mM-4 (22 kPa in compression), 65 mM-5 (30 kPa in compression) and glass controls. Significant differences were found between the softest gels, 65 mM-3 and 50 mM-5, and the stiffest, 65 mM-4 and 65 mM-5, and with glass controls (Fig. 5(b)). Conversely, cell spreading in the two latter conditions showed no statistical difference with cell spreading on glass controls. Similarly to previous observations on substrates with close ligand spacing,[4,12] hMSC spreading increased together with the substrate Young's modulus, as stiffer substrates promote integrin clustering, the development of higher traction forces and stronger stress fibres, all leading to flatter and more spread morphologies. However, as shown in Fig. 5(b), once the substrate's E reaches a threshold value – the stiffness of 65 mM-4 gels, approximately 22 kPa – the cell area reaches a plateau, as integrin clustering and force application cannot increase indefinitely.[4] Accordingly, cells showed more elongated shapes on 65 mM-3 gels, with significantly different aspect ratios than on the other conditions (Fig. 5(c)). As hydrogel stiffness increased for 50 mM-5, cell shape became more polygonal and the aspect ratio decreased, remaining higher than that observed on the stiffer gels (65 mM-4 and 65 mM-5) and controls, among which we found no significant differences in the cell aspect ratio. Cells exhibited spread, polygonal morphologies closer to the typical shape of differentiating osteoblasts. Cell shape is an important indicator of differentiation, as the cytosolic tension developed during spreading regulates the nuclear translocation of mechanotransduction systems like YAP/TAZ, which activate transcription factors associated with cell differentiation pathways in response to substrate stiffness.[3,6,77] Looking at cell proliferation (shown in phase contrast images in Fig. S14A–E, ESI†) and final cell densities, illustrated by cell counts per field of view (Fig. 5(d)), it can be seen that cells proliferated more on hydrogel with increasing stiffness. Overall, cells reached confluency between 4 and 7 days after seeding. The highest cell density was found on glass controls and was significantly different from the ones on 65 mM-3, 50 mM-5 and 65 mM-4 gels. Increasing cell contractility, stiffer substrates can favour the assembly of the cytoskeletal machinery necessary for cell division, thus favouring cell proliferation.[78] These results show that substrate mechanics can also influence long-timescale cell processes, such as cell proliferation or differentiation.

So, we next evaluated hMSC osteogenic differentiation by quantifying the nuclear levels of osteopontin (OPN), a protein highly expressed in differentiating bone cells and osteoblasts. The lowest expression values were observed in hMSCs seeded on glass controls lacking the BMP-2 biomimetic peptides and on the two softest conditions, 65 mM-3 and 50 mM-5. The BMP-2 is an osteoinductive factor that binds to BMPRI-II and activates, in an integrin-dependent pathway,[30] Smad downstream signalling, promoting the nuclear translocation of the transcription factor Runx-2 and inducing the expression of various osteogenic proteins, including osteopontin.[55] Interestingly, hMSCs seeded on glass only received the osteogenic factors supplemented with culture medium and, despite showing spread and polygonal morphologies, expressed low OPN levels, indicating that traditional culture conditions induce limited cell differentiation (Fig. 5(e)). On 65 mM-3 and 50 mM-5 gels, OPN expression was not different from controls. This indicates that the combination of GRGDSPC and BMP-2 bp has a limited effect on hMSC osteogenic differentiation in relatively soft hydrogels (below 14 kPa in this case), where hMSCs might lack the correct actomyosin organisation for the osteogenic differentiation.[17]

OPN levels increased on stiffer gels, with almost a two-fold rise on 65 mM-5 (compared to control levels) and more than a two-fold increase on 65 mM-4 gels, with significant differences from the levels observed on 50 mM-5 and 65 mM-5 gels (Fig. 5(e)). Interestingly, the gel in which we observed the highest OPN expression, 65 mM-4, is close to the optimal range reported in the literature for the best osteogenic differentiation of hMSC on 2D scaffolds (27 ± 10 kPa).[12,33] The average Young's modulus of this gel was approximately 22 kPa at the macroscale and 80 kPa in AFM nanoindentation after functionalisation.[16,17,70] On the other hand, the average Young's modulus of 65 mM-5 hydrogels (where we observed the second-highest OPN expression) was measured as 30 kPa at the macroscale but 112.2 ± 29.29 kPa in AFM after functionalisation, at the upper limit of the commonly indicated E range.[12,32] Collectively, these results confirm earlier literature reports of the influence of substrate stiffness on the osteogenic differentiation of hMSCs, and particularly the absence of a monotonic increase in cell differentiation with increasing substrate stiffness. In addition, these findings also demonstrate the challenge of defining an absolute range of Young's modulus values for stem cell differentiation on bioactive surfaces (in 2D).

For this reason, other physical parameters are now considered to decipher hMSC mechanosensitive responses, such as the cell traction forces necessary to activate the mechanotransduction pathways controlling cell adhesion, spreading and differentiation to specific cell lineages.[4,13,79] Our results demonstrate that for the same density of GRGDSPC and BMP-2 biomimetic peptides (approximately 2 pmols mm^{-2}) immobilised on the surface of hydrogels, mesenchymal stem cells achieve a more pronounced differentiation towards the osteogenic lineage in elastic, DGL G5-PEG hydrogels with stiffness of 22–30 kPa, in agreement with the observations on polyacrylamide[16] and alginate[15] hydrogels.

Conclusions

We demonstrated, for the first time, that dendrigrafts of poly-L-lysine of fifth generation (DGL-G5) can be used to crosslink biomimetic PEG hydrogels for hMSC osteogenic differentiation without eliciting cytotoxic responses. Interestingly, the high availability of reactive amines on DGL G5 allowed us to control the network crosslinking density and graft a combination of GRDGSPC and BMP-2-mimicking peptides independently from hydrogel stiffness. Moreover, a maleimide-PEG-NHS spacer ensured the selective coupling of the Cys-containing peptides at the terminal cysteine. Therefore, this study paves the way for using dendrigrafts of high generation as hydrogel crosslinkers. In particular, dendrigraft functionalisation with other chemical groups, not explored here, can potentially allow the tuning of the hydrogel stress relaxation, opening new synthetic strategies in the biomaterials field.

Author contributions

Michele Valeo: conceptualisation, formal analysis, investigation, validation, writing – original draft, visualisation. Sébastien Marie: methodology, writing – review and editing; Murielle Rémy: methodology, validation; Tiphaine Menguy: methodology, investigation; Cédric Le Coz: methodology; Michael Molinari: methodology, writing – review and editing; Cécile Feuillie: methodology, validation, writing – review; Fabien Granier: writing – review and editing, funding acquisition, project administration; Marie-Christine Durrieu: conceptualisation, investigation, formal analysis, ressources, writing – review and editing, supervision, project administration, funding acquisition.

Data availability statement

The data supporting this article have been included as part of the ESI.† Further experimental data are available upon request.

Conflicts of interest

The authors of the present paper declare no conflicts of interest.

Acknowledgements

The authors thank Anthony Vial and Sandrine Villette from the VibrAFM platform at CBMN (University of Bordeaux) for the AFM and IR experiments. The authors thank Laurent Garelly, Laura Guée, Noémie Brissi, Paul Reynaud, Marie Berger of FGHI for their involvement in this project. Finally, the authors thank Artem Zibarov, Evgeny Aspartin, Cristina Lopez (CBMN, University of Bordeaux) and Francesco Giacomarra (University of Trieste) for their help. Financial support from the ANR (ANR-21-CE06-0031-02) (M. C. D.) is also acknowledged.

References

1 P. Kanchanawong and D. A. Calderwood, Organization, dynamics and mechanoregulation of integrin-mediated cell–ECM adhesions, *Nat. Rev. Mol. Cell Biol.*, 2023, **24**, 142–161.
2 J. Z. Kechagia, J. Ivaska and P. Roca-Cusachs, Integrins as biomechanical sensors of the microenvironment, *Nat. Rev. Mol. Cell Biol.*, 2019, **20**, 457–473.
3 A. Saraswathibhatla, D. Indana and O. Chaudhuri, Cell–extracellular matrix mechanotransduction in 3D, *Nat. Rev. Mol. Cell Biol.*, 2023, **24**, 495–516.
4 R. Oria, *et al.*, Force loading explains spatial sensing of ligands by cells, *Nature*, 2017, **552**, 219–224.
5 K. Adebowale, *et al.*, Enhanced substrate stress relaxation promotes filopodia-mediated cell migration, *Nat. Mater.*, 2021, **20**, 1290–1299.
6 H. De Belly, E. K. Paluch and K. J. Chalut, Interplay between mechanics and signalling in regulating cell fate, *Nat. Rev. Mol. Cell Biol.*, 2022, **23**, 465–480.
7 C. F. Guimarães, L. Gasperini, A. P. Marques and R. L. Reis, The stiffness of living tissues and its implications for tissue engineering, *Nat. Rev. Mater.*, 2020, **5**, 351–370.
8 B. Xue, *et al.*, Engineering hydrogels with homogeneous mechanical properties for controlling stem cell lineage specification, *Proc. Natl. Acad. Sci. U. S. A.*, 2021, **118**, e2110961118.
9 M. F. Pittenger, *et al.*, Mesenchymal stem cell perspective: cell biology to clinical progress, *npj Regener. Med.*, 2019, **4**, 22.
10 P. Bianco, *et al.*, The meaning, the sense and the significance: translating the science of mesenchymal stem cells into medicine, *Nat. Med.*, 2013, **19**, 35–42.
11 K. H. Vining and D. J. Mooney, Mechanical forces direct stem cell behaviour in development and regeneration, *Nat. Rev. Mol. Cell Biol.*, 2017, **18**, 728–742.
12 B. Trappmann, *et al.*, Extracellular-matrix tethering regulates stem-cell fate, *Nat. Mater.*, 2012, **11**, 642–649.
13 M. Zhang, *et al.*, Controllable ligand spacing stimulates cellular mechanotransduction and promotes stem cell osteogenic differentiation on soft hydrogels, *Biomaterials*, 2021, **268**, 120543.
14 S. Li, *et al.*, Stiffness and BMP-2 Mimetic Peptide Jointly Regulate the Osteogenic Differentiation of Rat Bone Marrow Stromal Cells in a Gelatin Cryogel, *Biomacromolecules*, 2024, **25**(2), 890–902.
15 N. Huebsch, *et al.*, Harnessing traction-mediated manipulation of the cell/matrix interface to control stem-cell fate, *Nat. Mater.*, 2010, **9**, 518–526.
16 A. J. Engler, S. Sen, H. L. Sweeney and D. E. Discher, Matrix Elasticity Directs Stem Cell Lineage Specification, *Cell*, 2006, **126**, 677–689.
17 O. F. Zouani, J. Kalisky, E. Ibarboure and M. C. Durrieu, Effect of BMP-2 from matrices of different stiffnesses for the modulation of stem cell fate, *Biomaterials*, 2013, **34**, 2157–2166.
18 A. S. Rowlands, P. A. George and J. J. Cooper-White, Directing osteogenic and myogenic differentiation of MSCs: interplay of stiffness and adhesive ligand presentation, *Am. J. Physiol.: Cell Physiol.*, 2008, **295**, C1037–C1044.
19 W. T. Hsieh, *et al.*, Matrix dimensionality and stiffness cooperatively regulate osteogenesis of mesenchymal stromal cells, *Acta Biomater.*, 2016, **32**, 210–222.

20 H. F. Pereira, I. F. Cengiz, F. S. Silva, R. L. Reis and J. M. Oliveira, Scaffolds and coatings for bone regeneration, *J. Mater. Sci.: Mater. Med.*, 2020, **31**, 27.

21 S. R. Caliari and J. A. Burdick, A practical guide to hydrogels for cell culture, *Nat. Methods*, 2016, **13**, 405–414.

22 C. C. Lin and K. S. Anseth, PEG hydrogels for the controlled release of biomolecules in regenerative medicine, *Pharm. Res.*, 2009, **26**, 631–643.

23 J. Lou and D. J. Mooney, Chemical strategies to engineer hydrogels for cell culture, *Nat. Rev. Chem.*, 2022, **6**, 726–744.

24 A. S. Mertgen, *et al.*, Multifunctional Biomaterials: Combining Material Modification Strategies for Engineering of Cell-Contacting Surfaces, *ACS Appl. Mater. Interfaces*, 2020, **12**, 21342–21367.

25 E. Migliorini, A. Valat, C. Picart and E. A. Cavalcanti-Adam, Tuning cellular responses to BMP-2 with material surfaces, *Cytokine Growth Factor Rev.*, 2016, **27**, 43–54.

26 A. Saito, Y. Suzuki, S. Ogata, C. Ohtsuki and M. Tanihara, Activation of osteo-progenitor cells by a novel synthetic peptide derived from the bone morphogenetic protein-2 knuckle epitope, *Biochim. Biophys. Acta, Proteins Proteomics*, 2003, **1651**, 60–67.

27 X. He, J. Ma and E. Jabbari, Effect of Grafting RGD and BMP-2 Protein-Derived Peptides to a Hydrogel Substrate on Osteogenic Differentiation of Marrow Stromal Cells, *Langmuir*, 2008, **24**, 12508–12516.

28 O. F. Zouani, C. Chollet, B. Guillotin and M. C. Durrieu, Differentiation of pre-osteoblast cells on poly(ethylene terephthalate) grafted with RGD and/or BMPs mimetic peptides, *Biomaterials*, 2010, **31**, 8245–8253.

29 A. W. James, *et al.*, A Review of the Clinical Side Effects of Bone Morphogenetic Protein-2, *Tissue Eng., Part B*, 2016, **22**, 284–297.

30 L. Fourel, *et al.*, β3 integrin–mediated spreading induced by matrix-bound BMP-2 controls Smad signaling in a stiffness-independent manner, *J. Cell Biol.*, 2016, **212**, 693–706.

31 Y. Zhang, M. Remy, T. Leste-Lasserre and M.-C. Durrieu, Manipulating Stem Cell Fate with Disordered Bioactive Cues on Surfaces: The Role of Bioactive Ligand Selection, *ACS Appl. Mater. Interfaces*, 2024, **16**, 18474–18489.

32 E. Prouvé, *et al.*, Interplay of matrix stiffness and stress relaxation in directing osteogenic differentiation of mesenchymal stem cells, *Biomater. Sci.*, 2022, **10**, 4978–4996.

33 F. Posa, *et al.*, Surface Co-presentation of BMP-2 and integrin selective ligands at the nanoscale favors α5β1 integrin-mediated adhesion, *Biomaterials*, 2021, **267**, 120484.

34 N. M. Moore, N. J. Lin, N. D. Gallant and M. L. Becker, Synergistic enhancement of human bone marrow stromal cell proliferation and osteogenic differentiation on BMP-2-derived and RGD peptide concentration gradients, *Acta Biomater.*, 2011, **7**, 2091–2100.

35 I. Bilem, *et al.*, RGD and BMP-2 mimetic peptide crosstalk enhances osteogenic commitment of human bone marrow stem cells, *Acta Biomater.*, 2016, **36**, 132–142.

36 L. E. Jansen, L. Negron-Pineiro, S. Galarza and S. R. Peyton, Control of Thiol-Maleimide Reaction Kinetics in PEG Hydrogel Networks, *Acta Biomater.*, 2018, **70**, 120–128.

37 C. C. Lin, Recent advances in crosslinking chemistry of biomimetic poly(ethylene glycol) hydrogels, *RSC Adv.*, 2015, **5**, 39844–39853.

38 S. Grube and W. Oppermann, Inhomogeneity in hydrogels synthesized by thiol-ene polymerization, *Macromolecules*, 2013, **46**, 1948–1955.

39 C. Ghobril, E. K. Rodriguez, A. Nazarian and M. W. Grinstaff, Recent Advances in Dendritic Macromonomers for Hydrogel Formation and Their Medical Applications, *Biomacromolecules*, 2016, **17**, 1235–1252.

40 S. Kaga, M. Arslan, R. Sanyal and A. Sanyal, Dendrimers and Dendrons as Versatile Building Blocks for the Fabrication of Functional Hydrogels, *Molecules*, 2016, **21**(4), 497.

41 D. A. Tomalia, *et al.*, A New Class of Polymers: Starburst-Dendritic Macromolecules, *Polym. J.*, 1985, **17**, 117–132.

42 F. Granier, *et al.*, Assessment of Dendrigrafts of Poly- L -lysine Cytotoxicity and Cell Penetration in Cancer Cells, *ACS Appl. Polym. Mater.*, 2022, **4**, 908–919.

43 A. Janaszewska, J. Lazniewska, P. Trzepiński, M. Marcinkowska and B. Klajnert-Maculewicz, Cytotoxicity of Dendrimers, *Biomolecules*, 2019, **9**, 330.

44 S. J. Buwalda, *et al.*, Ultrafast in situ forming poly(ethylene glycol)-poly(amido amine) hydrogels with tunable drug release properties via controllable degradation rates, *Eur. J. Pharm. Biopharm.*, 2019, **139**, 232–239.

45 X. Bi, *et al.*, Polyamidoamine dendrimer-PEG hydrogel and its mechanical property on differentiation of mesenchymal stem cells, *Biomed. Mater. Eng.*, 2019, **30**, 111–123.

46 Y. Wang, Q. Zhao, H. Zhang, S. Yang and X. Jia, A novel poly(amido amine)-dendrimer-based hydrogel as a mimic for the extracellular matrix, *Adv. Mater.*, 2014, **26**, 4163–4167.

47 H. Collet, *et al.*, An Expeditious Multigram-Scale Synthesis of Lysine Dendrigraft (DGL) Polymers by Aqueous N-Carboxyanhydride Polycondensation, *Chem. – Eur. J.*, 2010, **16**, 2309–2316.

48 J.-P. Francoia, J.-C. Rossi, G. Monard and L. Vial, Digitizing Poly-L-lysine Dendrigrafts: From Experimental Data to Molecular Dynamics Simulations, *J. Chem. Inf. Model.*, 2017, **57**(9), 2173–2180.

49 B. Romestand, *et al.*, Dendrigraft Poly-L-lysine: A Non-Immunogenic Synthetic Carrier for Antibody Production, *Biomacromolecules*, 2010, **11**, 1169–1173.

50 G. Coussot, *et al.*, Colorimetric quantification of amino groups in linear and dendritic structures, *Polym. Int.*, 2009, **58**, 511–518.

51 J.-C. Rossi, *et al.*, Functionalisation of free amino groups of lysine dendrigraft (DGL) polymers, *Tetrahedron Lett.*, 2012, **53**, 2976–2979.

52 M. Carrancá, *et al.*, Versatile lysine dendrigrafts and polyethylene glycol hydrogels with inherent biological properties: in vitro cell behavior modulation and in vivo biocompatibility, *J. Biomed. Mater. Res., Part A*, 2021, **109**, 926–937.

53 S. Roumani, *et al.*, Osteogenic Potential of a Polyethylene Glycol Hydrogel Functionalized with Poly-Lysine Dendrigrafts (DGL) for Bone Regeneration, *Materials*, 2023, **16**, 862.

54 L. Griveau, *et al.*, Design and characterization of an in vivo injectable hydrogel with effervescently generated porosity for regenerative medicine applications, *Acta Biomater.*, 2022, **140**, 324–337.

55 F. Long, Building strong bones: molecular regulation of the osteoblast lineage, *Nat. Rev. Mol. Cell Biol.*, 2012, **13**, 27–38.

56 C. J. G. Abrego, *et al.*, Multiscale Characterization of the Mechanical Properties of Fibrin and Polyethylene Glycol (PEG) Hydrogels for Tissue Engineering Applications, *Macromol. Chem. Phys.*, 2022, **223**, 1–9.

57 B. Unal and R. C. Hedden, Gelation and swelling behavior of end-linked hydrogels prepared from linear poly(ethylene glycol) and poly(amidoamine) dendrimers, *Polymer*, 2006, **47**, 8173–8182.

58 F. Della Sala, *et al.*, Mechanical behavior of bioactive poly(ethylene glycol) diacrylate matrices for biomedical application, *J. Mech. Behav. Biomed. Mater.*, 2020, **110**, 103885.

59 N. R. Richbourg and N. A. Peppas, The swollen polymer network hypothesis: Quantitative models of hydrogel swelling, stiffness, and solute transport, *Prog. Polym. Sci.*, 2020, **105**, 101243.

60 Z. Zhang, *et al.*, Synthesis of Poly(ethylene glycol)-based Hydrogels via Amine-Michael Type Addition with Tunable Stiffness and Postgelation Chemical Functionality, *Chem. Mater.*, 2014, **26**, 3624–3630.

61 J. M. Zuidema, C. J. Rivet, R. J. Gilbert and F. A. Morrison, A protocol for rheological characterization of hydrogels for tissue engineering strategies, *J. Biomed. Mater. Res., Part B*, 2014, **102**, 1063–1073.

62 G. Stojkov, Z. Niyazov, F. Picchioni and R. K. Bose, Relationship between structure and rheology of hydrogels for various applications, *Gels*, 2021, **7**(4), 255.

63 M. Schweikle, T. Zinn, R. Lund and H. Tiainen, Injectable synthetic hydrogel for bone regeneration: Physicochemical characterisation of a high and a low pH gelling system, *Mater. Sci. Eng., C*, 2018, **90**, 67–76.

64 W. Megone, N. Roohpour and J. E. Gautrot, Impact of surface adhesion and sample heterogeneity on the multiscale mechanical characterisation of soft biomaterials, *Sci. Rep.*, 2018, **8**, 1–10.

65 M. Galluzzi, *et al.*, Space-resolved quantitative mechanical measurements of soft and supersoft materials by atomic force microscopy, *NPG Asia Mater.*, 2016, **8**, e327.

66 M. D. A. Norman, S. A. Ferreira, G. M. Jowett, L. Bozec and E. Gentleman, Measuring the elastic modulus of soft culture surfaces and three-dimensional hydrogels using atomic force microscopy, *Nat. Protoc.*, 2021, **16**, 2418–2449.

67 A. K. Denisin and B. L. Pruitt, Tuning the Range of Polyacrylamide Gel Stiffness for Mechanobiology Applications, *ACS Appl. Mater. Interfaces*, 2016, **8**, 21893–21902.

68 A. M. Abazari, S. M. Safavi, G. Rezazadeh and L. G. Villanueva, Modelling the Size Effects on the Mechanical Properties of Micro/Nano Structures, *Sensors*, 2015, **15**, 28543–28562.

69 D. Lee and S. Ryu, A Validation Study of the Repeatability and Accuracy of Atomic Force Microscopy Indentation Using Polyacrylamide Gels and Colloidal Probes, *J. Biomed. Eng.*, 2017, **139**(4), 044502.

70 M. Lanniel, *et al.*, Substrate induced differentiation of human mesenchymal stem cells on hydrogels with modified surface chemistry and controlled modulus, *Soft Matter*, 2011, **7**, 6501–6514.

71 C. M. Madl, M. Mehta, G. N. Duda, S. C. Heilshorn and D. J. Mooney, Presentation of BMP-2 Mimicking Peptides in 3D Hydrogels Directs Cell Fate Commitment in Osteoblasts and Mesenchymal Stem Cells, *Biomacromolecules*, 2014, **15**, 445–455.

72 A. Farrukh, J. I. Paez, M. Salierno and A. del Campo, Bioconjugating Thiols to Poly(acrylamide) Gels for Cell Culture Using Methylsulfonyl Co-monomers, *Angew. Chem., Int. Ed.*, 2016, **55**, 2092–2096.

73 S. Lee, A. E. Stanton, X. Tong and F. Yang, Hydrogels with enhanced protein conjugation efficiency reveal stiffness-induced YAP localization in stem cells depends on biochemical cues, *Biomaterials*, 2019, **202**, 26–34.

74 Y. Zhang, *et al.*, Controlling differentiation of stem cells via bioactive disordered cues, *Biomater. Sci.*, 2023, **11**, 6116–6134.

75 Y. Ma, *et al.*, Concentration-Dependent hMSC Differentiation on Orthogonal Concentration Gradients of GRGDS and BMP-2 Peptides, *Biomacromolecules*, 2016, **17**, 1486–1495.

76 M. Sun, *et al.*, Effects of Matrix Stiffness on the Morphology, Adhesion, Proliferation and Osteogenic Differentiation of Mesenchymal Stem Cells, *Int. J. Med. Sci.*, 2018, **15**, 257–268.

77 S. Dupont, *et al.*, Role of YAP/TAZ in mechanotransduction, *Nature*, 2011, **474**, 179–183.

78 P. A. Janmey, D. A. Fletcher and C. A. Reinhart-King, Stiffness Sensing by Cells, *Physiol. Rev.*, 2020, **100**, 695–724.

79 P. Han, *et al.*, Five Piconewtons: The Difference between Osteogenic and Adipogenic Fate Choice in Human Mesenchymal Stem Cells, *ACS Nano*, 2019, **13**, 11129–11143.